Ionics (2021) 27:3461–3475
https://doi.org/10.1007/s11581-021-04107-9

ORIGINAL PAPER

Three-dimensional CFD modeling of H_2/O_2 HT-PEMFC based on H_3PO_4-doped PBI membranes

A. R. Q. Panesi[1] · R. P. Silva[1] · E. F. Cunha[1] · I. Korkischko[1] · E. I. Santiago[1]

Received: 13 January 2021 / Revised: 30 April 2021 / Accepted: 17 May 2021 / Published online: 5 June 2021

Abstract

A complete non-isothermal model of a HT-PEMFC setup using a PBI/ H_3PO_4 membrane was developed, modeled, and solved using COMSOL Multiphysics. Polarization curves were simulated and compared to the corresponding experimental data. In this work, a serpentine flow field and an active area of 5 cm^2 have been implemented in a computational fluid dynamics (CFD) application. The model predicts water vapor transport, mass concentration of H_3PO_4, temperature, and membrane current density distribution. In this model, the anode feed is pure hydrogen, and oxygen is introduced at the cathode side. The heat transfer model was coupled with the electrochemical and mass transport; a particular heating configuration is investigated for temperature distribution, emphasizing the membrane. The models showed consistency and were used to investigate the behavior of H_3PO_4 concentration and all transport characteristics. The concentration of phosphoric acid decreases with increasing temperature and relative humidity and the diffusive flux of water vapor increases with the decrease of the operating voltage. Two different configurations of inlet and outlet flow channels were analyzed and the results were compared.

Keywords HT-PEMFC · PBI · CFD · Phosphoric acid

Introduction

Among the several fuel cell types, the proton exchange membrane fuel cells, also known as PEM fuel cells or PEMFC, are expected to play a significant role in the next-generation energy systems. Particularly the PEM fuel cell working at high temperature was developed to solve the main problems of a conventional, low temperature, namely, CO poisoning of the Pt catalyst and water management in both the gas diffusion layer and the membrane [1].

Depending on the working temperature, PEM fuel cells can be classified into two categories: low-temperature proton exchange membrane (LT-PEMFC) and high-temperature proton exchange membrane (HT-PEM). LTPEMFC is part of the group that works with an operating at temperatures below 100 °C with a high degree of external humidity as a consequence of the need of providing water, which acts as a proton carrier and it is fundamental in proton conduction mechanisms of typical perfluorosulfonic acid membranes used as the solid-state electrolyte of these devices. The transport properties of the proton exchange membrane are highly sensitive to heat coupling with water content [2]. On the other hand, HT-PEMFCs (operating temperature ranging from 100 to 200 °C) usually use membranes based on polybenzimidazole (PBI) and other aromatic amines doped with phosphoric acid as an electrolyte, whose proton transport mechanisms are completely independent of water, thus making it possible to operate in dry conditions.

By taking into account that the electrochemical reactions are thermoactivated processes, HT-PEMFC technology can be considered a very promising alternative over LT-PEMFC due to the following: (i) acceleration of rate-limiting reactions, (ii) increasing CO tolerance, (iii) absence of external humidification, (iv) simplified water management [3]. In particular, the acceleration of electrochemical reactions and the increase in CO tolerance provide an expansion of options for use as fuels—currently limited to pure hydrogen—such as hydrogen produced from hydrocarbon reform, methanol, and ethanol, which in general have a high concentration of by-products highly susceptible to poison Pt-based surfaces. Regarding operational dry conditions, the absence

✉ A. R. Q. Panesi
ricardopanesi@yahoo.com.br

[1] Nuclear and Energy Research Institute (IPEN-CNEN), Center of Fuel Cells and Hydrogen (CCCH), São Paulo, SP, Brazil

of complex external humidification systems can lead to simplified and practical prototypes [4].

In principle, phosphoric acid–doped PBI membranes are electrolytes in which proton conduction mechanisms are not water-dependent, considering that the proton-promoting species of such membranes are based on acid doping and not in an inherent ionomeric characteristic, which is typical in Nafion electrolytes. In addition, HT-PEMFCs are usually meant to run on the on-site produced reformate gas which can contain large amounts of water vapor. Also, the water produced from ORR on cathodic interface can result in some modifications in the properties of PBI-based electrolyte, mainly associated with lixiviation of H_3PO_4 dopant, altering the concentration and, as a consequence, the conductance of such membranes [5].

In the case of modeling studies, most of the efforts have been focused over the last 20 years on typical PEMFCs, i.e., LT-PEMFCs based on Nafion membranes, while research on HT-PEMFCs with PBI membrane has been considerably recent, having its beginning approximately 12 years ago [6]. Although there have been various numerical investigations on HT-PEMFCs, most of them are based on an isothermal model and with few studies on temperature distribution and phosphoric acid in the membrane.

In this context, this work aims at the validation of high-performance HT-PEMFC based on H_3PO_4-doped PBI membranes operating by using computation fluid dynamics (CFD) numerical model. Prior to numerical analysis, the optimization of operational conditions was conducted in order to evaluate the influence of such parameters on the beginning-of-life HT-PEMFC performance and make a correlation between performance and water transport, temperature distribution analysis, current density distribution, and the mass concentration of H_3PO_4, which are the features considered in the numerical analysis. A variety of studies have been done on the impact of the different geometric variables of the flow channels on different operating aspects of the PEMFC. Recent studies analyzed the influence of cross-sectional configuration of the flow channel and the effect of the relative position of the anode and cathode flow [7].

The need of greater efficiency in flow channels has received considerable attention in the fuel cell community over the last two decades. There are two simple criteria for the design of a channel. One is to uniformly distribute gas reactants and diffuse them uniformly along channels to the CL through the GDL. Another issue is water and thermal management [8]. McGarry and Grega [9] studied the effects of inlet mass flow distribution and magnitude on gas reactant distribution for PEM fuel cells and the partially and fully developed inlet profiles were found to have the largest percentage of cells that are deficient, 20% at a flow rate of 6.05 g/s. Barreras et al. [10] indicated the effects of inlet angles on the flow distribution. Their results showed the importance of entrance effects in flow field designs. Lobato et al. [11] compared three flow fields: mixed, parallel, and pin-type. They observed that the mixed flow field gave the best performance. However, the pin-type configuration could actually be comparable to the mixed serpentine only at high current densities. As for pressure drop, the serpentine configuration has the highest-pressure drop compared to the parallel and pin-type flow channels.

Scott et al. [12] improved a high-temperature fuel cell with PBI membrane condensed by phosphoric acid in a one-dimensional and steady-state. In this research, the effect of operating pressure and cell temperature on the open circuit potential and the effect of diffusion coefficients, exchange current density, and water transport across the membrane on the conductivity of the PBI membrane were examined. Their results are consistent with experimental data.

Caglayan et al. [13] developed a three-dimensional and isothermal modeling for an HT-PEMFC. A triple-mixed serpentine flow channel single-cell with PBI membrane was applied for the model. The model was defined in steady-state, isothermal, and single-phase and simulated for different operating temperatures in the range of 100 to 180 °C. The results show that the increase in temperature has improved the performance of the fuel cell and the temperature influence on high-temperature performance is more pronounced between 100 and 120 °C than between 160 and 180 °C. Also, the distribution of current density at different voltages was investigated, and it was deduced that at higher operating voltages, local flow density is more uniform. Pressure drop contours and distribution of oxygen concentration along the gas flow channel were also evaluated.

In this paper, a three-dimensional, non-isothermal model for PEM fuel cell at high operating temperature ($T \geq 393$ K) is presented to describe the processes occurring in components of a fuel cell. Mathematical modeling is essential for the development of fuel cells because it gives the designer a better understanding of the effect of design and operating parameters on performance and operation. This work contributes to research on HT-PEMFC, mainly in the phenomena of temperature distribution, phosphoric acid in the membrane, and water vapor diffusion. Great attention has been given to numerical modeling, due to its important role in the study of fuel cells, since it is possible to quantify the moment, mass, and heat transfers, where it is neither possible and nor practicable to verify experimentally. In this way, modeling can help to understand what really happens inside fuel cells, support the research of experimental activities and assist in the design and optimization of commercial systems. With this in mind, the main objective of this work is to

investigate the effect of how the fuel inlet and outlet channels working on hydrogen, by the same token, inedited results were obtained mainly in the phenomena of temperature distribution and phosphoric acid in the membrane in the HT-PEMFC.

Methodology

Synthesis of H_3PO_4-doped PBI membranes

PBI films were synthesized by the casting process of commercial PBI powders (Celazone®, PBI Performance Products INC.). The powders were previously dissolved in *N*,*N* dimethylacetamide (DMAc, 4 wt %, Aldrich) in the presence of lithium chloride (2 wt %) in an autoclave system at 250 °C for 6 h. More details can be found elsewhere [14]. After that, the resulting solution was filtered under vacuum for the elimination of polymer residues, excess of solvents, and non-dissolved PBI powders and then transferred to aluminum mold followed by heat treatment at 120 °C during 5 h in order to promote the solvent elimination and formation of the membrane (casting process). The resulting PBI membranes were exhaustively treated in 0.5 M H_2SO_4 solution for 1 h followed by two consecutive baths in ultrapure water at 80 °C for 1 h [14].

The doping process consisted of immersion of the membrane in 10 M H_3PO_4 (orthophosphoric acid, 85%, Merck) solution for 5 days at room temperature (~ 25 °C). The doping degree was determined by mass variation between non-doped and doped PBI membranes.

The gas diffusion electrodes (GDEs) were composed of independent diffusion layer (GDL) and catalyst layer (CL). The diffusion layer was prepared by deposition of a mixture of carbon powder (Vulcan XC72-R, Cabot) and Teflon (PTFE, TE-306A, DuPont) on a carbon fabric (ELAT LT 1400). Then, a highly homogeneous catalytic layer was produced by depositing a mixture of electrocatalyst (Pt / C, 20% by weight, BASF) and PBI powders previously doped with H_3PO_4 onto diffusion layer via automated spray (Ultra-Coat, Prisma 400). The Pt/C and PBI loadings on both anode and cathode were 0.4 mg.cm^{-2} and 30 wt %, respectively.

The membrane-electrodes assemblies (MEA) were prepared by hot pressing of anode to cathode onto the membrane at 125 °C and 1000 kgf.cm^{-2} for 2 min.

All tests were conducted at steady-state conditions at cell temperature setting of 180 °C. Pure H_2 and O_2 were fed to single cell at room temperature. The polarization curves were obtained galvanostatically. After cell temperature and OCV (open circuit voltage) stabilization, the current was applied ranging from 0.01 to 0.1 A with a current step of 0.01 A, 0.2 to 2.0 A with a step of 0.1 A, 2.2 to 10 A with a step of 0.2 A, and 10 to 15 A with a step of 0.5 A. All potential values were collected after 10 s at applied current. The OCV was collected after 5 min of stabilization. In order to evaluate the reproducibility of the system, 5 (five) polarization curves were obtained in sequence and the last one was employed in the numerical study. However, our HT-PEMFC test protocol includes running currents vs. potential data by using short time intervals, but with subsequent runs until overlapping polarization curves are obtained, which ensure that the system has reached the steady state. The polarization curves employed in the numerical study were the last one, in general obtaining after 7 polarization curve runs, which must be necessarily stable. In order to validate the model, for the H_2 and O_2 flows, the stoichiometry ratio is 2 for both the anode and cathode, which correspond to volumetric fluxes of 164 and 86 mL.min^{-1}, respectively. Figure 1 shows the layout of gas flow channels studied in both models.

Model development

Using computational fluid dynamics (CFDs) software, models can be evaluated in numerical investigation of the water and current flow phenomena involved in fuel cell tests. Moreover, mathematical models can be perceived as critical tools, which can be beneficial for the comprehension and investigation of the areas which pose as challenges to the HT-PEMFC technology.

In particular to this analysis, modeling and simulation were performed in the COMSOL Multiphysics 5.3a software, which was used to build a single-phase non-isothermal and tridimensional fuel cell model with finite element method. For this model, the following conditions were assumed: steady state, ideal gas mixtures, fluid compressible, laminar flow, and electro-osmotic drag were

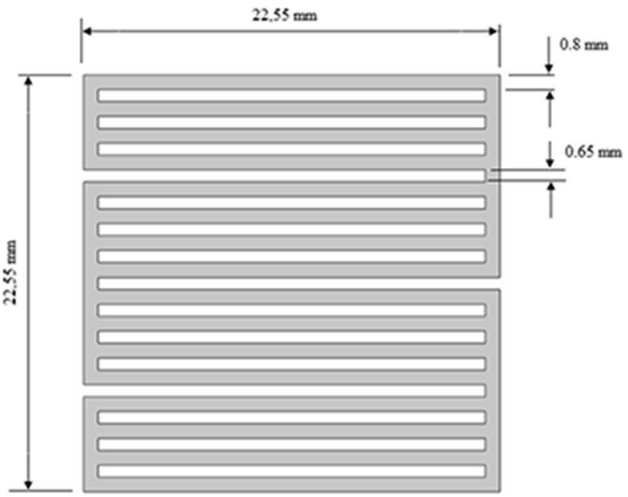

Fig. 1 Layout of gas flow channels for both models

considered negligible. Commercial software COMSOL Multiphysics is the second most used computational tool in the literature for modeling fuel cells and adequate for three-dimensional and non-isothermal numerical analysis as proposed in this study. For example, Kamal et al. [15] developed modeling studies using COMSOL Multiphysics simulating the thermal behavior of a partial cell inspired by a steady state heating configuration selected from a typical HT-PEMFC cell. The model indicates that operating parameters such as inlet gas temperatures of the anode and cathode affect the temperature distribution of the cell and the membrane. Similarly, Gülsah et al. [16] studied the effects of temperature on the transport of heat, mass, and charge occurring in the PEM fuel cell of phosphoric acid–doped polybenzimidazole membrane, assisted by COMSOL Multiphysics. Consequently, the results of this study clearly show the effects of temperature on heat, mass, and charge transports in the PBI-based PEM fuel cell.

The calculation domain consisted of gas channels, gas diffusion layers (GDLs), catalytic layers (CLs), membrane (mem), and bipolar plates (BPs), as seen in Fig. 2.

Three distinct physical domains are considered (see Fig. 2): the "main" domain composed of all regions, wherein the heat transfer is solved; domain 1, composed of the gas channels, porous GDL, and catalytic layers, in which mass and momentum transfer are considered; and domain 2 in the electrolyte, wherein only mass transfer is solved. This paper investigates the steady-state transport of reactants and water vapor in a cell including both anode and cathode mass and momentum transport phenomena in the flow channels, gas diffusion layers (GDLs), and porous electrodes, as well as electrochemical currents in the GDLs, the porous electrodes, and the PBI membrane. Also, the secondary current distribution interface in COMSOL is used to model the electrochemical currents

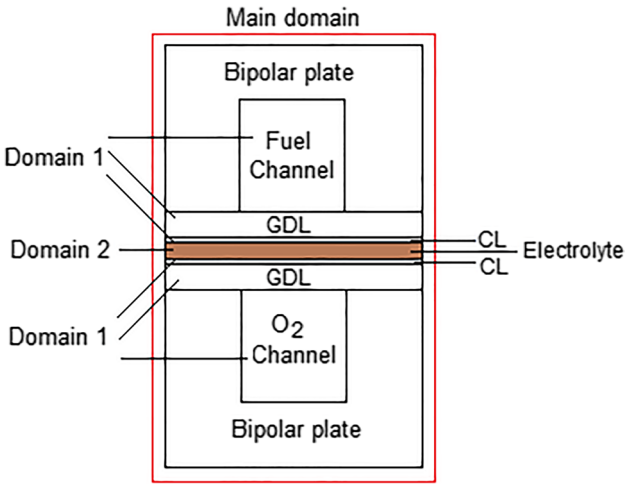

Fig. 2 Cross-section of a single channel pair

Table 1 Geometrical parameters of the model

Parameter	Value (mm)
Flow channel length	22.55
Flow channel width	0.8
Flow channel height	1.0
Rib width	0.65
Monopolar plate thickness	11
GDL thickness	0.454 [17]
Catalyst layer thickness	0.012
Membrane thickness	0.035

using Ohms law and solving for in the GDLs, in the porous electrodes, and in the electrolyte membrane.

The dimensions of the cell components with 5 cm^2 active area serpentine flow field are listed in Table 1. Furthermore, the parameters considered in the development of models are represented in Table 2.

Two models were developed taking into account different gas inlet/outlet positions in flow channels as illustrated in Fig. 3. The serpentine flow plate design in fuel cells has been investigated by several researchers around the world and it is considered the standard for flow design in most fuel cells. The simulations were made to develop an understanding of the fluid flow in the plates for different positions of the gas inlet/outlet channels. The flow direction of fuel gas in the anode channel is opposite to that of reactant gas in the cathode channel for both models are indicated in this figure and which are denoted as anode gas inlet, anode gas outlet, cathode gas inlet, and cathode gas outlet, respectively.

General equations

Mass and momentum conservation

In a fuel cell, there is mass transferred through the system in the form of hydrogen, oxygen, and water. Reactant flow in the fuel cell flow channels is dependent upon the design of the channels. In the electrode and membrane layers, the reactants may transfer via convection and diffusion. Regardless of the method of transport, the governing equations are still the same [35]. The general equation for mass conservation, which inside a fuel cell such as fluid flow, diffusion and phase change is:

$$\frac{\partial \rho}{\partial t} + \nabla\left(\rho \vec{V}\right) = 0 \tag{1}$$

Since the models are steady state, we can neglect the transient terms in all model equations. The first term represents the accumulation of mass with time, and the second term describes the net flow of mass out of the element across its boundaries and is called the convective

Table 2 Physiochemical and transport properties

Parameter	Value
Membrane conductivity	2.7 Sm^{-1}
Electronic conductivity in the GDL, BP	66,700 [18], 3000 Sm^{-1}
Permeability of GDL, CL	1.18×10^{-11} m^2, 10^{-13} m^2 [19]
Volume fraction of electrolyte in CL	0.55 [20]
Thermal conductivities of GDL, CL, membrane, BP	1.2, 1.5, 0.95, 20 W m^{-1} K^{-1} [15, 21, 22]
Reference exchange current density at anode	1×10^{5} Am^{-2} [23–25]
Reference exchange current density at cathode	1.8×10^{-4} Am^{-2} [26, 27]
Cathodic Tafel slope	100 $mVdec^{-1}$ [28, 29]
Anode transfer coefficient	0.5 [30]
Cathode transfer coefficient	1.0 [16, 31]
Pt loading	0.004 kgm^{-2}
Acid doping level	120%
Density of GDL, CL, membrane, BP	1743.8, 1000, 1300, 1580 kg m^{-3} [23–25]
Operating pressure and temperature	101.325 kPa, 453.15 K
Porosity of GDL, CL	0.8, 0.25
Specific heat capacities of GDL, CL, membrane, BP	568, 3300, 1650, 1580 J kg^{-1} K^{-1} [6–8]
Diffusion of O_2 in H_3PO_4	1.65×10^{-9} m^2 s^{-1}[21, 32–34]
Diffusion of H_2 in H_3PO_4	3.31×10^{-9} m^2 s^{-1}[21, 32–34]
H_2 -H_2O Binary diffusion coefficient	4.85×10^{-5} m^2 s^{-1}[27]
O_2 -H_2O Binary diffusion coefficient	3.80×10^{-5} m^2 s^{-1}[27]

term. The conservation of momentum is required to model the fluid velocity and species partial pressures. Momentum conservation for fluid compressible is described by flow channels:

$$\frac{\rho}{\varepsilon}\left(\frac{\partial\vec{V}}{\partial t}+\left(\vec{V}\nabla\right)\right)\frac{\vec{V}}{\epsilon}=-\nabla p+\nabla\left[\frac{\mu}{\epsilon}\left(\nabla\vec{V}+\left(\nabla\vec{V}\right)^{T}-\frac{2}{3}\left(\nabla\cdot\vec{V}\right)I\right)\right]-\left(\frac{\mu}{k}+\beta\left|\vec{V}\right|+\frac{S_{\phi}}{\epsilon^{2}}\right)\vec{V}+F \tag{3}$$

$$\frac{\partial\left(\rho\vec{V}\right)}{\partial t}+\nabla\left(\rho\vec{V}\vec{V}\right)=-\nabla p+\nabla\left[\mu\left(\nabla\vec{V}+\left(\nabla\vec{V}\right)^{T}-\frac{2}{3}\left(\nabla.\vec{V}\right)\mathrm{I}\right)\right]+S_{m} \tag{2}$$

The Brinkman Eq. (3) describes the gas flow within the porous medium, i.e., GDL and CL. This mathematical model extends Darcy's law to include a term that accounts for the viscous transport in the momentum balance, and it treats both the pressure and the flow-velocity vector as independent variables:

The left side of Eq. (2) describes the accumulation of momentum with time and the second term describes advection momentum flux. On the right side, the first term represents the pressure gradient and the second term viscous stress tensor. The source term S_m is different for different regions of the fuel

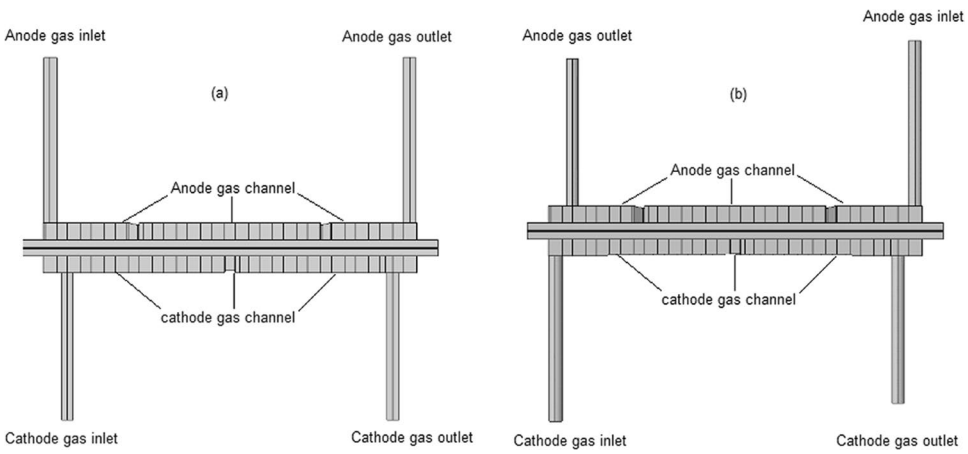

Fig. 3 Models developed in COMSOL Multiphysics: **a** model A, **b** model B

cell, ρ and $\overrightarrow{V}$ denote the mixture density and superficial fluid velocity respectively, μ is the dynamic viscosity, ε is the porosity, and k is the permeability of the porous medium.

Species conservation

The transport of species both at the anode and at the cathode is given by the advection equation, together with the definition of the total mass flux N_i for each species i of the mixture:

$$\frac{\partial}{\partial t}\left(\epsilon\rho\omega_i\right) + \nabla\left(\epsilon\rho\omega_i\overrightarrow{V}\right) = -\nabla.J_i + S_s \tag{4}$$

$$N_i = J_i + \rho\overrightarrow{V}\omega_i \tag{5}$$

The first two terms in the species conservation equation represent species accumulation and advection terms, and the first term on the right-hand side represents Fickian diffusion of species in porous medium. In Eq. (4), ω_i is the mass fraction of species and J_i is the diffusion flux. The source term S_s is equal to zero everywhere except in the catalyst layers where the species are consumed or generated in the electrochemical reactions. The diffusion model adopted on the anode side as on the cathode was Fick's law model with the following equations:

$$J_i = -\left(\rho D_i^{fk}\nabla\omega_i + \rho\omega_i D_i^{fk}\frac{\nabla \mathrm{M}}{M} + D_i^T\frac{\nabla T}{T}\right) \tag{6}$$

where D_i^T is the thermal diffusion coefficient and the effective diffusivity D_i^{fk} are obtained through:

$$D_i^{fk} = \left(\frac{1}{D_i^f} + \frac{1}{D_i^k}\right)^{-1} \tag{7}$$

In addition, D_i^{fk}, which represents a general diffusion matrix (SI unit: m^2s^{-1}), can be described the diffusion of species i into the mixture and the Knudsen diffusion coefficient, respectively:

$$D_i^f = \frac{1-\omega_i}{\sum_{k\neq i}\chi_{k/D_{ejk}}} \tag{8}$$

$$D_i^k = \frac{\lambda_i}{3}\sqrt{\frac{8RT}{\pi M_i}} \tag{9}$$

where D_{ejk} are the binary diffusion coefficients, and λ is the mean free path average distance a particle travels between collisions.

The diffusivity of oxygen in PBI is related to oxygen diffusivity in phosphoric acid and acid doping level. Thus, it can be given as [21, 32–34]:

$$D_{O_2}^{PBI} = \left(\epsilon_{PBI}\right)^{1,8} D_{O_2}^{H_{3PO_4}} \tag{10}$$

where ϵ_{PBI} is the volume fraction of electrolyte in CL. The transport properties of oxygen in concentrated phosphoric acid are related to the temperature and the acid concentration mass fraction ($m_{H_{3PO_4}}$):

$$D_{O_2}^{H_{3PO_4}} = 10^{-9} exp\left[\frac{-192{,}55\left(m_{H_{3PO_4}}\right)^2 + 323{,}55\left(m_{H_{3PO_4}}\right) - 125{,}61 + 62010\left(m_{H_{3PO_4}}\right)^2 - 105503\left(m_{H_{3PO_4}}\right) + 40929}{T}\right] \tag{11}$$

As a result of insufficient studies on hydrogen solubility and diffusion in hot phosphoric acid, the diffusion coefficient cannot be correlated to experimental data. Thus, it was assumed that these parameters behave in the same way as in water systems:

$$D_{H_2}^{PBI} = \left(\epsilon_{PBI}\right)^{1,8} 2D_{O_2}^{H_{3PO_4}} \tag{12}$$

The diffusivity values of oxygen and hydrogen in phosphoric acid are important parameters to be considered and are required by the software in the "porous medium transport properties." The diffusion coefficient of oxygen through water vapor is in several orders of magnitude larger than through liquid water. With increasing operating temperature, the ratio of liquid water to water vapor inside cathode catalyst layers and gas diffusion layers decreases. This will serve to increase the effective diffusion coefficient of oxygen. Therefore, high-temperature operation facilitates oxygen transport through the gas diffusion layers and the cathode catalyst layers.

Charge conservation

In the operation of fuel cells, two different types of electrical charges are present: protons H^+ passing through the membrane and catalyst layer, and electrons e^- collected by the electrodes (catalyst layer and gas diffusion layer). Thus, an electronic potential (ϕ_{sol}) and a protonic potential (ϕ_{mem}) in different locations of the computational domain should be considered. The two potentials can be written as:

$$i + \left(\sigma_{sol}\nabla\phi_{sol}\right) - S_{sol} = 0 \tag{13}$$

$$i + \left(\sigma_{mem}\nabla\phi_{mem}\right) - S_{mem} = 0 \tag{14}$$

where potential "sol" is responsible for the transport of electrons through the solid materials of the electrode, and "mem" represents the potential transport of protons through the membrane; σ_{sol} and σ_{mem} are the electronic conductivities of the electrodes and ionic conductivity of the membrane, respectively. The source terms S_{sol} and S_{mem} represent the volumetric transfer current.

The currents generated j are the results of electrochemical reactions that occur in the catalytic layer next to the membrane, whose phenomenon depends on the potential difference between the solid matrix of the electrode and the membrane. For a reversible reaction at very low overpotential (η of order $RT/F \sim 25$ mV), the exponentials in the Butler-Volmer equation can be linearized:

$$j_a = j_{0a}\left[\frac{F}{RT}\left(a_a + a_c\right]\eta_a \right. \tag{15}$$

where α_{ac} are the cathode and anodic transfer coefficients.

Using a linearized Butler-Volmer reaction can be advantageous when investigating convergence issues of a model. The anodic overpotential η_a is given by:

$$\eta_a = \phi_s - \phi_l - E_{eq} \tag{16}$$

where E_{eq} is the equilibrium potential of the reaction and the subscript of the potentials are l for the electrolyte and s for the electrode respectively. The equilibrium potential of the electrode is zero on the anode side, and it equals the theoretical cell potential at aa given temperature and pressure on the cathode. The anodic and cathodic exchange current densities are given by:

$$j_{0a} = j_{0\text{aref}}\frac{P_{H2}}{P} \tag{17}$$

$$j_{0c} = j_{0\text{cref}}\frac{P_{O2}}{P} \tag{18}$$

where j_{0ref} is the reference electric current density, P_{H2} and P_{O2} are the partial pressure of hydrogen and oxygen, and P is the reference pressure. The cathodic kinetics can be expressed as:

$$j_c = -j_{0c} \times 10^{\eta_c/b} \tag{19}$$

where b is the Tafel coefficient.

Energy conservation

Operational temperature and heat generated dominate the reaction rate and can change the phase of the reactants. Therefore, it is essential to account for temperature distribution within the cell by solving the conservation of energy equation. The general form of conservation of energy in terms of temperature is given in Eq. (20):

$$\rho c_p \frac{\partial T}{\partial t} + \nabla\left(\rho c_p \vec{V} T\right) = \nabla\left(\mathrm{k}\vec{\nabla} T\right) + S_e \tag{20}$$

where T is operating temperature, c_p is the specific heat, k is the effective thermal conductivity, and S_e is the source term which includes the heat generated by the electrochemical reactions (that only exists in the catalyst layers), the ohmic heat due to the thermal resistance of the solid areas and the heat generated by the phase change process if any. At the free borders of the fuel cell, a convective flow condition has been defined:

$$-\text{n.q.} = h\left(\mathrm{T_{ext}} - \mathrm{T}\right) \tag{21}$$

where T_{ext} is ambient temperature and h is the average of heat transfer coefficient by convection. The average heat transfer coefficient was obtained by [36].

There are five source terms, S_m, S_s, S_e, S_{sol}, and S_{mem}, which represent various volumetric sources or sinks arising from each sub-region of a fuel cell. Details of the various source terms are summarized in Table 3.

The H_3PO_4 concentration within the MEA is expected to change during cell operation. In [37], a correlating equation for H_3PO_4 vapor pressure is given (80–101 wt % acid in the range of 130–170 °C). From their experimental data, Souza et al. [38] generated an equation that coupled concentration and water vapor partial pressure:

$$X_{H3PO4} = \frac{ln\left(P_{H2O}\right) + \frac{2765{,}1}{T} - 22.002}{-\frac{4121.9}{T} + 2.5929} \tag{22}$$

where P_{H2O} is the water vapor partial pressure and X_{H3PO4} is the mole fraction of H_3PO_4.

Table 3 Source terms for momentum, species, energy, and charge conservation equations in various regions of a fuel cell

	Flow channels	GDL	CL	Membrane
Momentum	$S_m = 0$	$S_m = -\frac{\mu}{k}\vec{V}\epsilon$	$S_m = -\frac{\mu}{k}\vec{V}\epsilon$	———
Species	$S_s = 0$	$S_s = 0$	$S_s = -j_a\frac{M_{H_2}}{4F}$ $S_s = j_c\frac{M_{O_2}}{4F}$	$S_s = 0$
Charge	$S_{sol} = 0$ $S_{mem} = 0$	$S_{sol} = 0$ $S_{mem} = 0$	$S_{sol} = -j_a$ $S_{sol} = j_c$ $S_{mem} = j_a$ $S_{mem} = -j_c$	$S_{sol} = 0$ $S_{mem} = 0$
Energy	$S_e = 0$	$S_e = 0$	$S_e = i_{0a}\left(\eta_a + T\frac{dE_{eq}}{dT}\right) + \frac{j_a^2}{k}$ $i_{0c}\left(\eta_c + T\frac{dE_{eq}}{dT}\right) + \frac{j_c^2}{k}$	$S_e = \frac{j^2}{k}$

Results and discussion

Figure 4 compares model predictions with the corresponding experimental data for a PEM fuel cell at 180 °C, showing a good agreement between the experimental and numerical curves. In both cases, the cell was operated at constant temperature and without any humidification. Oxygen was used at the cathode and hydrogen at the anode. Until 500 mV, a good agreement between experimental data and model results was obtained for both configurations and moving away from a little in the ohmic losses region. Below this potential, the performance predicted for each geometry was different. In general, model A gave a slightly best performance. From an open circuit to 600 mV, the potential rapidly decreased due to activation losses. This region is characterized by low current densities and a sharp decrease in voltage due to activation losses, mainly on the cathode side. Between 600 and 300 mV, the potential fell almost linearly with current density, as a result of ohmic losses, caused by ionic and electronic resistance. At potentials below 300 mV, there was a rapid fall in voltage. This was caused by mass transport limitations, in particular the oxygen diffusion in hot concentrated phosphoric acid. The value of oxygen diffusion coefficient given by Eq. (10) was very low for the entire range of potential (1.65×10^{-9} m^2 s^{-1}).

Temperature distribution analysis

The temperature distribution through the membrane is a very important consideration as it can give information about the real temperature in the center of the cell. It can be useful to predict possible problems concerning thermal stresses and hot spots, especially on the membrane surface. The heating strategy considered for the start-up of the HT-PEMFC is based on one of the common methods, i.e., the heat input flux refers to the external heat sinks that is required from the heating element (electrical resistances) to raise the maximum membrane temperature to reach 180 °C. Figure 5 shows the temperature distribution within the membrane where the anode and cathode gases inlet temperature are set at 293.15 K. In addition, it can be seen that there is a considerable difference in temperature between the central region and regions closer to the inlet and outlet of flow channels, indicating that the temperature distribution of the membrane is also governed by inlet gases temperature. Besides that, the region close to the cathode inlet shows a temperature of 130 °C for both models, while in the outlet, they are is very different, which is around 20 degrees higher for the value of outlet model B. At the same time, the region close to the anode shows the same temperature of inlet and outlet for both models. In fact, the lowest temperature occurs at the regions closer to the cathode inlet rather than the anode inlet. This is probably due to the lower thermal conductivity of oxygen relative to hydrogen. Thus, the consideration of the oxygen inlet temperature is more critical in context to increase the temperature to the desired level work, it should be indicated that the increase in the temperature is faster around the cathode inlet. Oxygen concentration is one of the most critical parameters affecting the current density. It decreases with the increased temperature and consumption due to the oxidation reaction taking place in the cathode as shown in Fig. 6. Further decrease is caused also by the

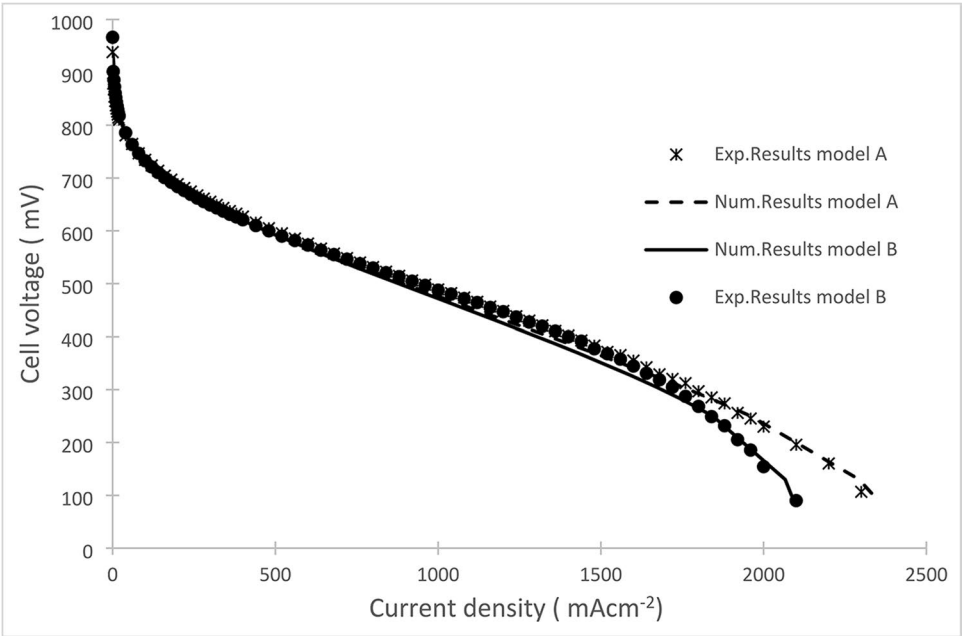

Fig. 4 Polarization curve: comparison of simulations and experiments

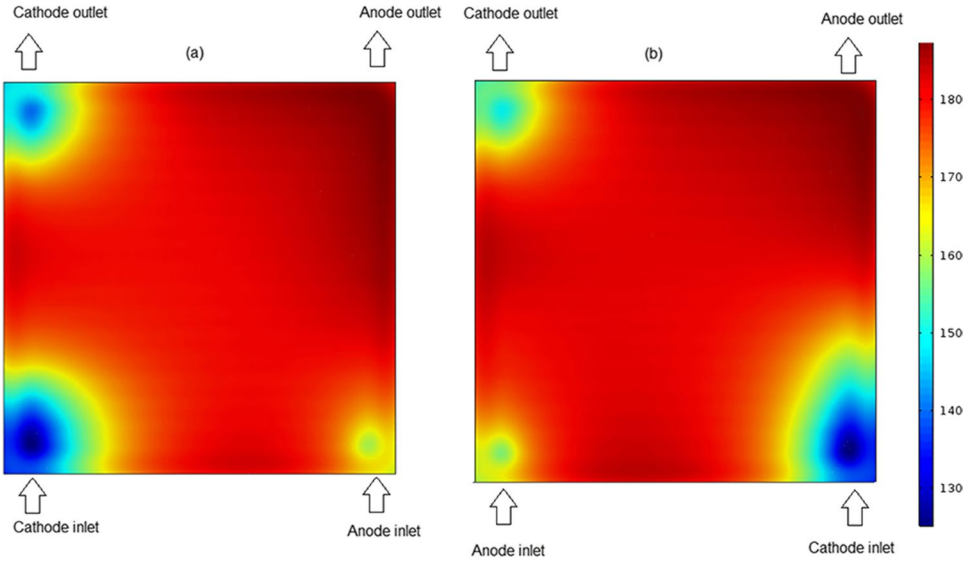

Fig. 5 Temperature distribution (in °C) in the middle of the membrane at 90 mV: **a** model A, **b** model B

increase in product water vapor. Therefore, an increase in the temperature around the cathode inlet is much more noticeable compared to the increase around the anode inlet, which is an expected result.

Water transport

Based on the assumption that due to the concentration gradient, water vapor can diffuse through the membrane, since water is produced in cathode, the diffusion of water is therefore usually from cathode side to anode side. The source terms S_s on the catalyst layer boundaries describe reactant consumption and water generation based on the electrochemical reactions (see Table 3). The transport of water vapor through the membrane is described by Fick's law of diffusion. On the other hand, anode flooding occurs less frequently due to several reasons. One main reason is the back diffusion of water from the cathode to the anode, especially when low hydration level of the hydrogen gas stream creates a force that is stronger than the electro-osmotic drag [26, 39]. The issue with liquid water is one of the major problems that have dominated research efforts in LT-PEMFCs. Therefore, water management in HT-PEMFCs does not need to be so closely controlled. Also, as the cell is operated at a higher temperature, the water can be considered in the vapor phase and the problems of liquid water blocking the catalyst pores and two-phase flow between gas and liquid are alleviated. When the PBI

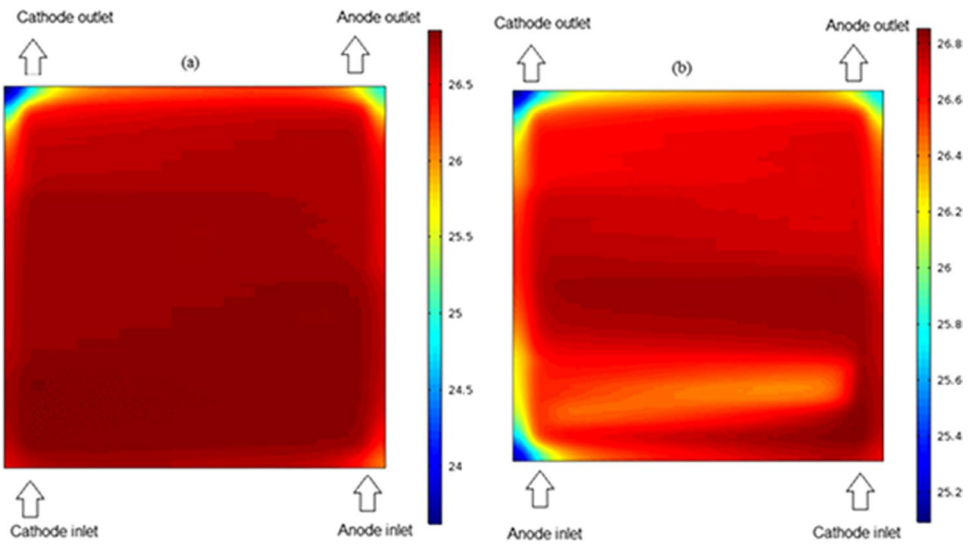

Fig. 6 Calculated O_2 mole concentration in the cathode catalyst layer/GDL interface at 90 mV: **a** model A, **b** model B

membrane is doped in phosphoric acid it can efficiently conduct protons even in anhydrous conditions. This eliminates the need for humidification and simplifies the system design by reducing water management issues [40]. The water vapor transport in PEMFCs occurs by three different modes, which are diffusion, electro-osmotic drag, and hydraulic permeability. The water transport in PBI membranes is carried out only by diffusion, due to no dominant effect of the other modes. The reasons for this are that there is no humidification requirement in PBI, hydraulic permeability is dominant at the different anode/cathode pressures, and liquid electrolyte phase and all species are in gas phases [13]. As for the water transport by diffusion ($kgm^{-2}\ s^{-1}$), Figs. 7 and 8 present water flow distribution due to the difference in concentration between the membrane faces at operating voltage 280 mV and 90 mV. Those potential values were selected for the analysis, due to represent extreme conditions of cell operation. For example, the loss of phosphoric acid is reported to be greatly affected by the operating current density, because the hydration status of the phosphoric acid is changed according to the amount of water generated at different current densities.

Detailed in Figs. 7 and 8, the water diffusion increases with the decrease of the operating voltage. This increase is due to the greater difference in water concentration at the membrane interfaces. Since the relative humidity of the gas stream in the cathode is often the highest at flow channel exit due to the accumulation of product water, the counter flow arrangement by placing the anode and cathode flows in opposite directions is widely used to enhance the water transport from cathode to anode. The water vapor concentration is higher in the outlet of the two models (anode and cathode side) than that in inlet due to two reasons. First, the temperature of inlet gases is relatively low, as time goes by the gases are absorbing heat when circulating through the flow channels. So in the middle zone near the flow channels, which is much hotter, the evaporation rate is the highest, and the generated water is less. Second, the inlet gases are non-humidified; since when it flows over the flow channels, it will absorb the heat water vapor. So the vapor partial pressure will rise, which will lead to the highest water fraction at the end of flow channels. Also, the water transport in the membrane is quite poor for its physical characteristics. Unlike the traditional proton exchange membrane, high temperature can conduct protons without liquid water. On the

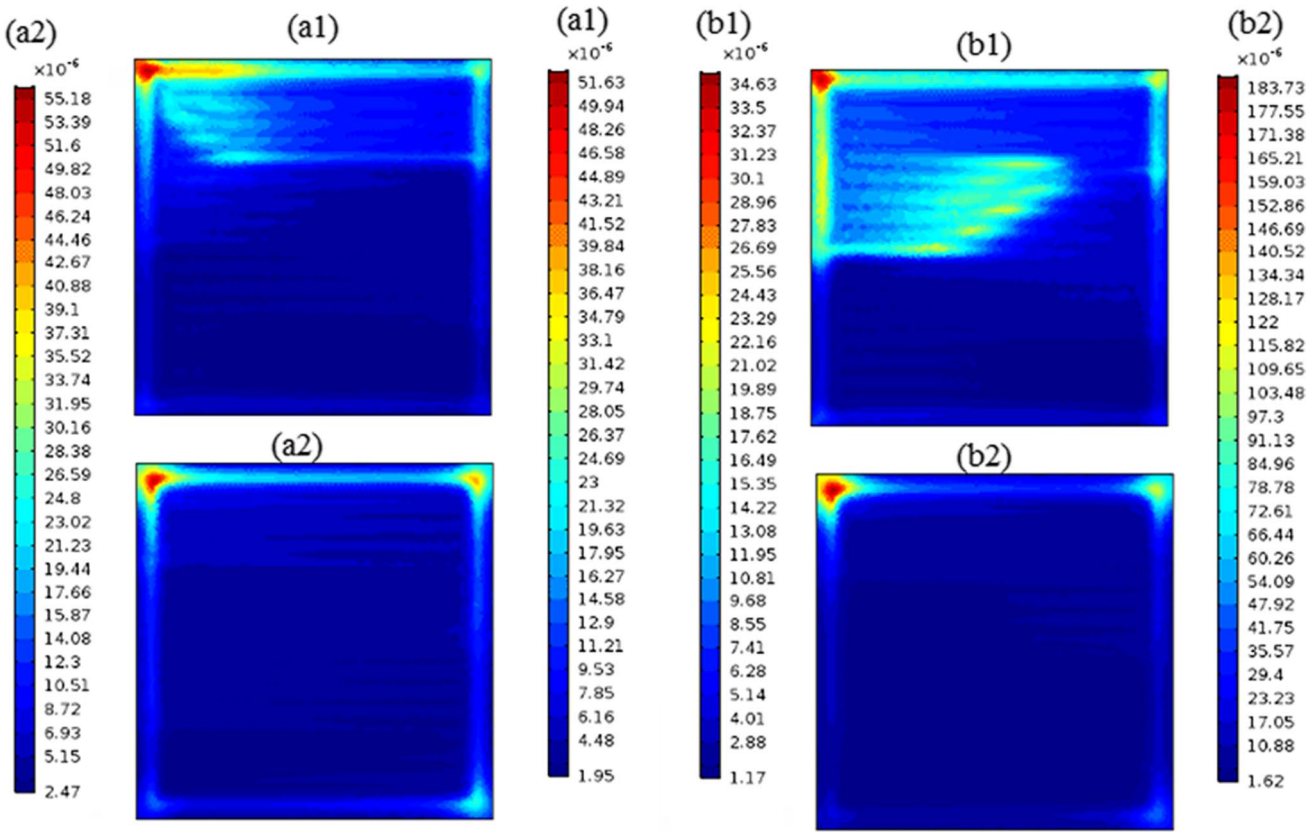

Fig. 7 Diffusive flux of water vapor along with the membrane model A: (a1) anode side 280 mV, (a2) anode side 90 mV, (b1) cathode side 280 mV, (b2) cathode side 90 mV

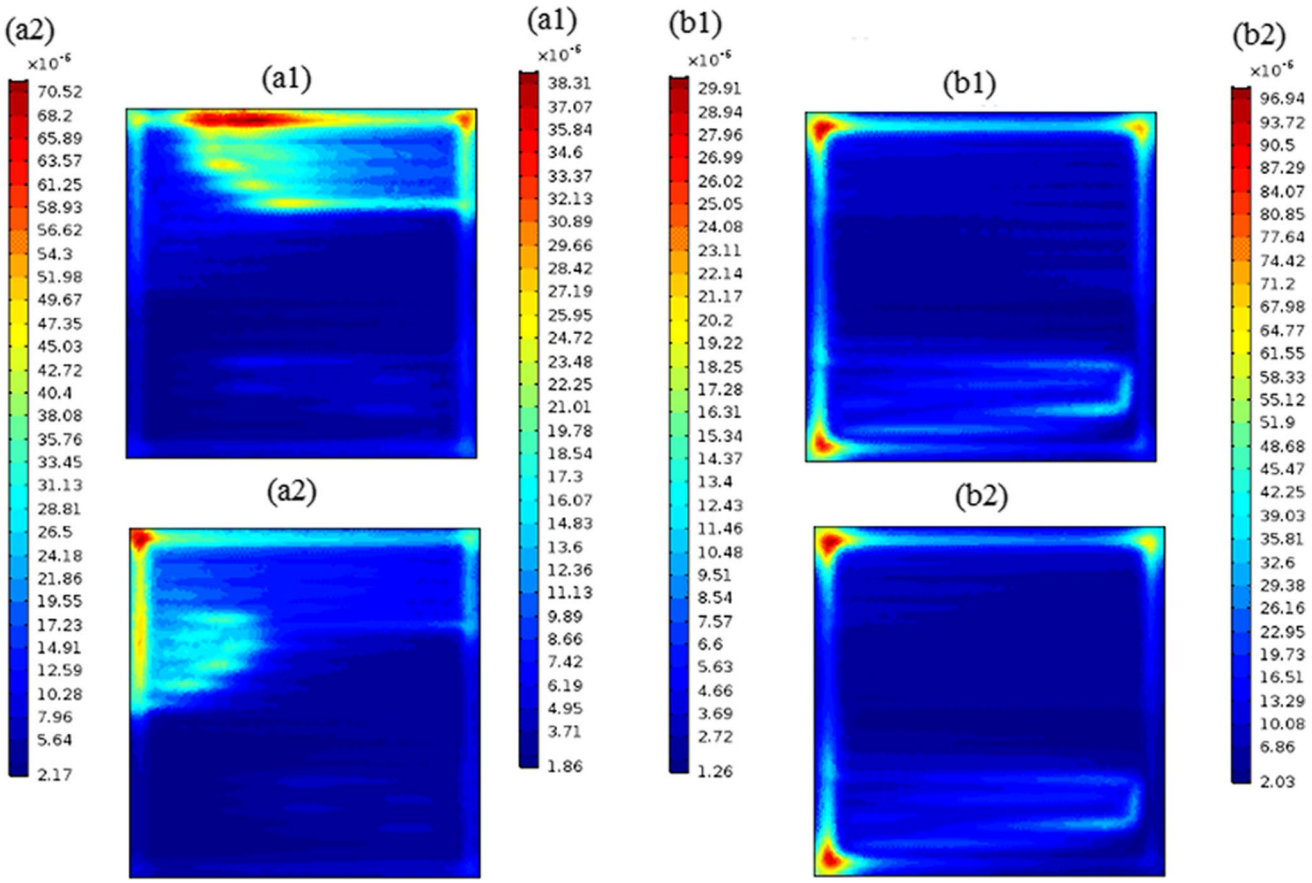

Fig. 8 Diffusive flux of water vapor along the membrane model B: (a1) anode side 280 mV, (a2) anode side 90 mV, (b1) cathode side 280 mV, (b2) cathode side 90 mV

other hand, it should be pointed out that the water produced in the anode zones at a potential of 90 mV is much lower than in the cathode from Figs. 7 and 8. More importantly, at 90 mV, there was less back diffusion in model A than in model B, causing a higher concentration of water on the cathode side of model A.

Current density distributions

Figures 9 and 10 show the current density distribution ($A.cm^{-2}$) in the middle of the membrane surface for a cell operated at base case operating conditions at 280 mV and 90 mV. As it is seen in such figures, there are some points at which the local current density has remarkably high values. All four illustrations have similar current density distributions, with model B showing a lower value for both potentials. As shown, the reaction did not occur uniformly through the membrane layer for both models at 280 mV. The maximum current density was obtained in the adjacent areas of the ribs, while mid-way between the ribs, the current density was low. It shows that the current density distribution does not follow the same characteristics when working at low temperatures (LT-PEMFC).

Despite that, the distribution of the oxygen mass concentration causes influence on the current density distribution. In general, at the exit of the cathode gas flow channel, the O_2 mole fraction decreases, and the water vapor mass fraction increases towards the cathode side outlet (oxygen dilution) (see Fig. 6). Additionally, the results are strongly influenced by the bipolar plate or flow-field structure. In contrast with potential 280 mV, the reaction rate was more uniform through the membrane layer, for potential at 90 mV. This different distribution between models probably was not caused by the electric resistance, but by mass transport limitations of oxygen molecules and did not possibly reach these areas easily.

Phosphoric acid distribution analysis

Highly concentrated phosphoric acid under STP is hydrophilic and tends to absorb water. Because of the varying humidity within a fuel cell, it is difficult to estimate the

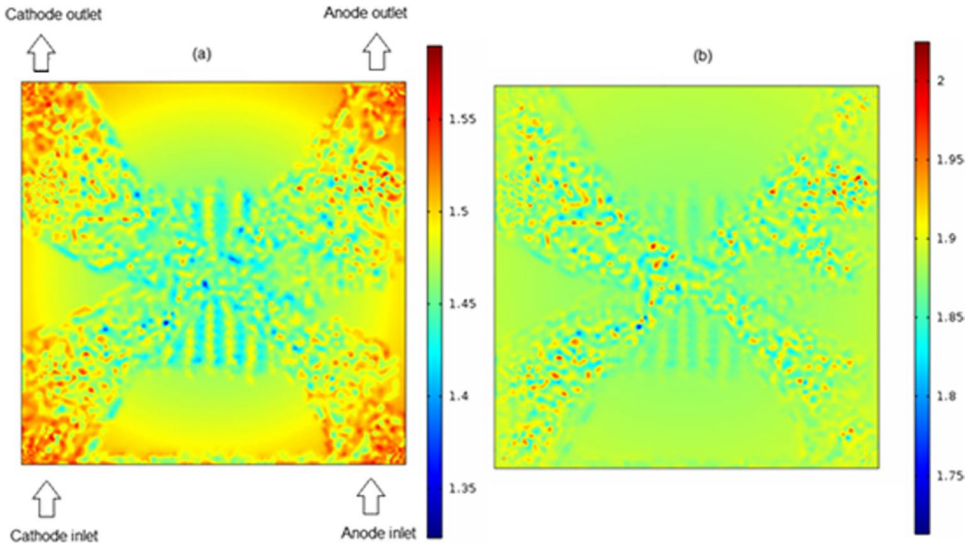

Fig. 9 Current density distributions in the middle of the membrane model A: **a** 280 mV, **b** 90 mV

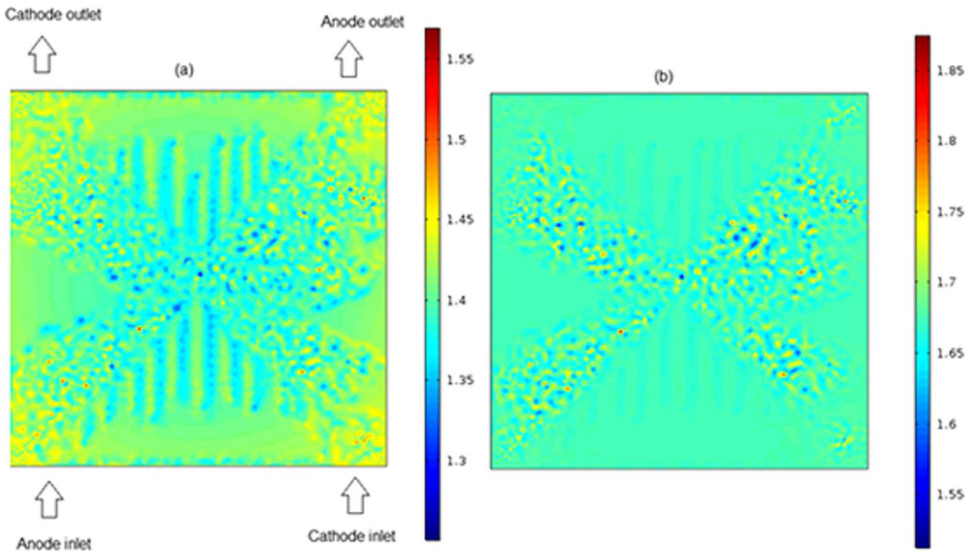

Fig. 10 Current density distributions in the middle of the membrane model B: **a** 280 mV, **b** 90 mV

in-situ concentration of phosphoric acid mixture. The concentration of H_3PO_4 depends on the temperature and on the relative humidity [41]. The highly concentrated phosphoric acid under normal conditions of temperature and pressure is hydrophilic and tends to absorb water. In the operation of the fuel cell at 180 °C, considerable portions of water vapor are produced, which leads to a probable dilution of the phosphoric acid. The models use an approach that couples the partial pressure of the water, the diffusivity of the gases, and the working temperature as indicated by Eqs. (10), (11), and (12) and that according to Siegel et al. [42], the H_3PO_4 concentration within the MEA is expected to change during cell operation.

As can be seen in Fig. 11 from Eq. (22), the mole fraction of phosphoric acid decreases with increasing temperature and relative humidity. This results from the temperature dependence of the vapor pressure of water over phosphoric acid. Combined with the actual partial pressure of water the vapor pressure is the driving force of the evaporation, hence the volume change. The influence of the doped acid and absorbed water on the volume swelling for acid-doped PBI membranes was studied and found the effect of swelling by water to be negligible [43]. Our model predicts the concentrations as shown in Fig. 11. At 90-mV cell voltage, the mole fraction, X_{H3PO4}, ranges from 0.79 to 0.87 for both models. The drier condition at the cathode side gas inlet increases the concentration of the H_3PO_4. Further at the cathode outlet, the flow channels contain more water vapor because of the higher rate of evaporation, as shown in Figs. 7 and 8. Moreover, from

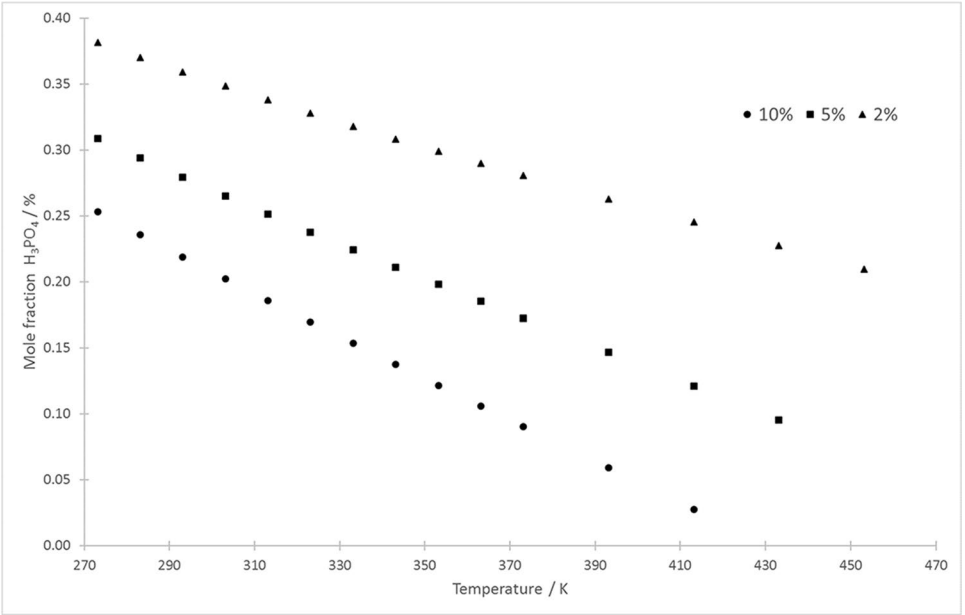

Fig. 11 Influence of the temperature and relative humidity on the mole fraction of H_3PO_4

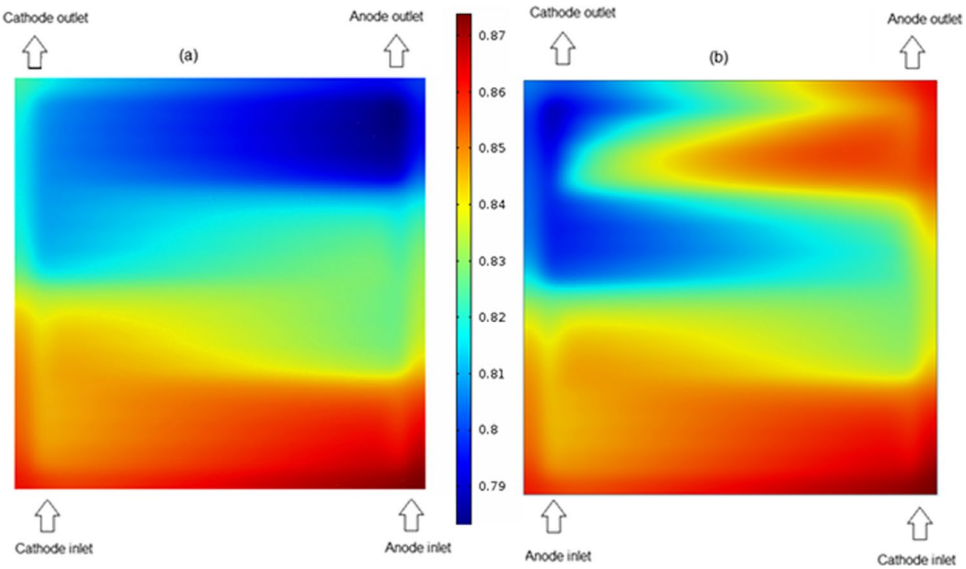

Fig. 12 Phosphoric acid mole fraction in the middle of the membrane at 90 mV: **a** model A, **b** model B

Fig. 12, it can be seen that the low values at the cathode side are located close to the outlet, where the highest temperature and water supply occur.

Conclusion

A complete non-isothermal model of a HT-PEMFC setup using a PBI/ H_3PO_4 membrane was developed, modeled, and solved using COMSOL Multiphysics 5.3a. Polarization curves were simulated and compared to the experimental data. Water was considered to be in the vaporous phase and the water transportation across the membrane from anode to cathode was ignored because of its low water electro-osmosis drag force. The models showed consistency and were used to investigate the behavior of H_3PO_4 concentration and all transport characteristics. Two different configurations of inlet and outlet flow channels (hydrogen and oxygen) were analyzed and the results were compared. It was found that alternating the oxygen gas inlet, there was an increase in the current density of the fuel cell in model A. Regarding the

effects of humidification, it is important to point out that the condition of the MEA is crucial for the result, obviously when diluted the ionic conductivity of PBI increases. Many publications observed the effects of humidification with differing system responses, such as [13, 26, 39, 40]. However, the concentration of phosphoric acid decreases with increasing temperature and relative humidity. Despite that, the simulation results show that promising cell performance can be obtained without humidification. The H_3PO_4 concentration values and the temperature influence in the gas diffusivity values were in good agreement with the values reported for hot concentrated H_3PO_4. The proposed HT-PEMFC model developed in this study has been shown to be an important tool for understanding the key physical and transport phenomena in fuel cells, and these findings can be further extended to guide the operation and design of high-temperature PEM fuel cell in practical applications. Nevertheless, much more experimental and theoretical work is necessary to precisely identify the interactions of H_3PO_4, PBI, and water vapor to develop a complete phosphoric acid transport model for continuous operation.

Abbreviations List of symbols

b: Tafel coefficient; c_p: Specific heat capacity/ J kg^{-1} K^{-1}; D_i^T : Thermal diffusion coefficient / m^2 s^{-1}; D_i^{fk}: Effective diffusivity / m^2 s^{-1}; D_{ejk}: Binary diffusion coefficient / m^2 s^{-1}; E_{eq}: Equilibrium potential / V; F: Faraday constant / 96,487 C mol^{-1}; h: Convective heat transfer coefficient / W m^{-2} K; j: Electronic current / A m^{-2}; j_0 : Exchange current density / A m^{-2}; $j_{0\text{ref}}$: Reference exchange current density / A m^{-2}; J_i: Diffusion flux / kg m^{-2} s^{-1}; k: Thermal conductivity / W m^{-1} K^{-1}; M: Molecular weight / kg mol^{-1}; $m_{H_{3PO_4}}$: Mass fraction of H_3PO_4; N_i: Total flux of species / kg m^{-2} s^{-1}; p : Pressure / Pa; R: Universal gas constant / 8.3143 J mol^{-1} K^{-1}; S_m: Source term for conservation of momentum / kg m^{-3} s^{-1}; S_s: Source term for conservation of species / mol m^{-3} s^{-1}; S_e: Source term for conservation of energy / W m^{-3}; S_{sol}: Source term for conservation of charge / A m^{-3}; S_{men}: Source term for conservation of charge / A m^{-3}; T: Temperature / K; X_{H3PO4}: Mole fraction of H_3PO_4

Greek symbols

α: Transfer coefficient; ε: Porosity; ε_{PBI}: Volume fraction of electrolyte in CL; η: Overpotential / V; I: Identity tensor; k: Permeability of the porous media / m^2; λ: Mean-free path average / nm; μ: Dynamic viscosity / Pa s; T: Transpose; ρ: Density / kg m^{-3}; σ: Conductivity / S m^{-1}; ϕ: Electric potential / V; ω_i: Mass fraction of species

Superscripts and subscripts

a: Anode; BP: Bipolar plate; c: Cathode; CL: Catalyst layer; ext: External; GDL: Gas diffusion layer; H_3PO_4: Phosphoric acid; H_2O: Water vapor; H_2: Hydrogen; l: Electrolyte; mem: Membrane; MEA: Membrane electrode assembly; O_2: Oxygen; PBI: Polybenzimidazole; STP: Standard conditions for temperature and pressure; sol: Solid phase excluding the membrane electrolyte; s: Electrode

Funding The authors are grateful for the support of the Center for Innovation on New Energies CINE-SHELL (ANP)/FAPESP (17/11937–4), the Research Center for Gas Innovating RCGI-SHELL (ANP)/FAPESP (14/50279–4), and the National Nuclear Energy Commission (CNEN). Thanks are also due to the funding supports from FAPESP 2014/09087–4. I.K. gratefully acknowledges the support from FAPESP (2016/12397–0).

References

1. Authayanun S, Im-orb K, Arpornwichanop A (2015) Chin J Catal 473:36
2. Shen J, Zeng L, Zhengkai Tu, Liu Z, Liu W (2019) J Porous Media 813:22
3. Savadogo O (2004) J Power Sources 235:135
4. Berna S (2016) Ankara: Middle East Technical University
5. Bezmalinović D, Strahl S, Roda V, Husar A (2014) Int J Hydrogen Energy 10627:39
6. Jaeman P, Kyoungdoug M (2012) J Power Sources 152:216
7. Morin Arnaud Xu, Feina GG, Oliver D (2011) Int J Hydrogen Energy 3096:36
8. Wang J (2015) Appl Energy 640:157
9. McGarry M, Grega L (2005) J Fuel Cell Sci Technol 45:3
10. Barreras F, Lozano A, Vali-no L, Mar in C, Pascau A (2005) J Power Sources 144:66
11. Lobato J, Canizares P, Rodrigo MA, Pinar FJ, Mena E, Úbeda D (2010) Int J Hydrogen Energy 5510:35
12. Scott K, Pilditch S, Mamlouk M (2007) J Appl Electrochem 1245:37
13. Caglayan DG, Berna S, Devrim Y, Eroglu I (2016) Int J Hydrogen Energy 10060:41
14. Silva RP (2019) Desenvolvimento de membranas não-fluoradas a base de PBI para aplicação em células a combustível de etanol direto de alta temperatura, IPEN
15. Rasheed RKA (2016) Siew Hwa Chan. Electrochim Acta 280:222
16. Elden G, Çelik M, Genç G, Yapıcı H (2016) Energy 772:103
17. Fuel Cell Store, Fuel Cell Modeling Basics, Material Information can be found under https://www.fuelcellstore.com/blog-section/fuel-cell-modeling-basics
18. ZOLTEK, Material Information can be found under https://pdf.directindustry.com/pt/pdf-en/zoltek/panex-30-brochure/38933-575644.html#open
19. Sohn Y-J, Kim M, Yang T-H, Kim K (2011) Int J Hydrogen Energy 15273:23
20. Huang H, Zhou Y, Hao Deng Xu, Du Xie Q, Yin Y, Jiao K (2016) Int J Hydrogen Energy 3113:41
21. Chippar P, Hyunchul Ju (2013) Int J Hydrogen Energy 7704:38
22. Chippar P, Hyunchul Ju (2012) Solid State Ionic 30:225
23. Xia L, Zhang C, Minghui Hu, Jiang S, Siong Chin C, Gao Z, Liao Q (2018) Int J Hydrogen Energy 23441:43
24. Wang Y, Sauer DU, Koehne S, Ersoez A (2014) Int J Hydrogen Energy 19067:39
25. Ubong EU, Shi Z, Wang X (2009) J Electrochem Soc B1276:156
26. Kamal R, Zhang C, Liao Q, Chan SH (2017) Int J Hydrogen Energy 3142:42

27. Yin Y, Wang J, Yang X, Qing Du, Fang J, Jiao K (2014) Int J Hydrogen Energy 13671:39
28. Siegel C, Lang S, Fontes E, Beckhaus P (2016) Springer International Publishing
29. MacDonald DI, Boyack JR (1969) Chem Eng Data 14:380–384
30. Siegel C High temperature polymer electrolyte membrane fuel cells: modeling, simulation, and segmented measurements
31. Cheddie DF, Munroe NDH (2007) Int J Hydrogen Energy 832:32
32. He R, Li Q, Bach A, Jensen J, Bjerrum N, Membr J (2006) J Membr Sci 38:277
33. Jiao K, Li X (2010) Fuel Cells 351:10
34. Liu H, Li P, Hartz A, Wang K (2015) Int J Energy Environ Eng 75:6
35. Su A, Ferng YM, Hou J, Yu TL (2012) Int J Hydrogen Energy 7710:9
36. Kreith F, Bohn MS, Thomson (2003)
37. Jiao K, Ibrahim Alaefour E, Li X (2011) Fuel 568:90
38. Sousa T, Mamlouk M, Scott K (2010) Fuel Cells 693:10
39. Jiao K (2011) Xianguo Li. Prog Energy Combust Sci 291:37
40. Araya SS, Zhou F, Liso V, Sahlin SL, Vang JR, Thomas S, Gao X, Jeppesen C, Kær SK (2016) Int J Hydrogen Energy 21310:41
41. Kazdal TJ, Lang S, Kühl F, Hampe MJ (2014) J Power Sources 446:249
42. Siegel C, Bandlamud G, Heiinzel A (2011) J Power Sources 2735:196
43. Sousa T, Mamlouk M, Scott K, Rangel CM (2012) Fuel Cells 566:12